ROV localization using ballasted umbilical equipped with IMUs

Juliette Drupt, Christophe Viel, Claire Dune, Vincent Hugel

ROV localization using ballasted umbilical equipped with IMUs

Juliette Drupt, Christophe Viel, Claire Dune, Vincent Hugel

***Abstract*—This article describes an affordable and setup-friendly cable-based localization technique for underwater Remotely Operated Vehicles (ROVs), which exploits the piecewise linear shape of the umbilical being equipped with a sliding ballast. Each stretched part of the cable is instrumented with a waterproof Inertial Measurement Unit (IMU) to measure its orientation. Using cable's geometry, the vehicle's location can be calculated in relation to the other fixed or moving end of the cable. Experiments carried out with a robotic system in a water tank prove the reliability of this localization strategy. The study investigates the influence of measurement uncertainties on cable orientation and length, as well as the impact of the IMU location along the cable on localization precision. The accuracy of the localization method is discussed.**

***Index Terms*—Underwater robotics, Cable model, Localization system.**

I. Introduction

UNDERWATER communication and localization are particularly challenging since Global Navigation Satellite System (GNSS) radio signals are immediately absorbed by the water. Remotely Operated Vehicles (ROVs) are underwater robots equipped with a cable, namely umbilical, that connects them to the surface to maintain bi-directional real-time communication, supply the robot with energy, but also maintain a lifeline with the robot to avoid losing it.

This communication scheme is essential to accomplish tasks that cannot be fully automated and require precision and adaptability, like wreck exploring or infrastructure inspection and maintenance. However, the umbilical is also subject to entanglement and its shape is difficult to predict, complicating the operator's task. Umbilicals are thus a tradeoff between these advantages and constraints. In line with [1], the current work aims at turning the presence of this physical link into an advantage by converting it into a localization system using a model of the umbilical and observing its shape. Geo-referenced localization of these robots is particularly important for the deployment and recovery of the robots, but also to locate the observations in the scientific missions.

In the absence of tension, a neutrally buoyant cable takes on an irregular shape, increasing the risk of entanglements with itself or its environment. In order to prevent these risks, a technique mostly used for shallow dives is to hang a ballast at a fixed length on the umbilical to stretch the cable portion between the boat and the ballast. If the ROV is close to the ballast, the cable between them takes the shape of a bell, similar to a catenary curve. However, when the ROV moves away from the ballast, the cable is straightened by the tension exerted by the ROV and ballast, and thus conforms into a three-dimensional straight line. A ballast tied to a cable can usually only stretch one part of it, the two parts in some particular configuration. However, a ballast moving freely along the cable, namely *sliding*, will always find its position at the lowest point, corresponding to its minimum of potential energy, where it stretches both parts of the cable simultaneously. The umbilical can then be assimilated to a piecewise linear model, making it particularly suitable for a cable-based ROV localization strategy.

Manuscript submitted in December 2023.

The contributions of the current work are the following:

- a new cable model that includes the shape of the pulley attached to the ballast,
- an implementation of a ROV's cable-based localization system using both cable-mounted IMUs, and ROV-mounted Initial Measurement Units (IMUs) and pressure sensor,
- a study of the influence of measurement errors on model parameter estimation and ROV localization accuracy,
- an experimental validation of ROV localization accuracy in test tanks i) for a fixed attachment point, by varying the position of the IMUs along the cable ii) for a mobile attachment point, attached to a second, manually-controlled ROV.

Related work on ROV localization and cable-based robot localization is presented in Section II. Section III presents the system under study including assumptions and cable system modelling. Embedded sensor-based model parameter measurement is detailed in Section IV. Experiments are presented in Section V to show the effectiveness of the approach and comments on the results obtained. Discussion and perspectives are exposed in Section VI, before concluding the current work in Section VII.

II. Related work

The geo-referenced localization of an underwater vehicle is usually obtained by locating the vehicle with respect to a reference point — generally, a surface station — with known GNSS coordinates.

In the last decade, the Underwater Wireless Sensor Networks (UWSNs) have received a lot of attention [2], [3]. UWSNs consist in several interacting components or nodes including vehicles and sensors which are deployed in a specific area in order to perform collaborative monitoring and data collection tasks. In such networks, the localization of a vehicle node can be deduced with respect to the other

components of the system, including anchors with known geo-referenced coordinates. An UWSN formed by a set of four anchors geo-localized anchors is studied and implemented in [4], [5]. Each anchor broadcasts ElectroMagnetic Waves (EMW) at specific frequencies, allowing the localization of a an underwater vehicle by using the received signal strength to approximate distances and angles to the anchor nodes. UWSNs are however limited by bandwidth restriction, important propagation delays between the nodes, power constraints, high cost due to the deployment of large sensor sets, as well as the need to calibrate the GNSS position of fixed anchors. In addition, the need to equip an area with fixed anchors restricts sea exploration to places where such sensor sets may be deployed.

Underwater vehicles geo-referenced localization is most usually performed by locating the vehicle with respect to a geo-referenced surface vessel using Ultra-Short Base Line (USBL). USBL positioning systems rely on an array of acoustic transducers placed under a ship and a transponder installed in the underwater vehicle. The pose of the robot can be estimated with respect to the boat by travel time and phase difference. USBL systems are lighter than UWSNs in terms of cost and constraints, since only two engines are implied in the localization process, namely the submarine robot and the surface vessel. USBL are therefore the most widely used systems for underwater vehicles geo-referenced localization. These systems are although still limited. Pose estimation accuracy is strongly affected by ocean environmental parameters and by sizing uncertainties of the transceiver array. Such systems are therefore highly dependent on a precise calibration. Pose estimation error increases with the distance between the boat and the vehicle: though USBL systems usually range down to 10,000 m, their ranging error is of 1 or 2% for most common systems, leading to poor vehicle localization accuracy in deep water [6], [7]. These systems are also limited by a low update rate due to travel duration of the acoustic waves. Consequently, USBL systems are generally used in a combination with additional embedded sensors including IMUs, cameras, pressure sensors or Sound Navigation and Ranging (SONAR) [8], [9].

Alternative approaches rely on vision for localization with respect to a fixed anchor with known GNSS coordinates. Usually, visual methods use characteristic patterns on the anchor for detection and relative localization [10], [11]. A limitation of these methods is the need to equip the seafloor with visual beacons, including the calibration of their relative and geo-referenced location. The performance of visual methods is also highly dependent on water turbidity and underwater visibility. These visual methods are therefore less common.

The specificity of the current work is to investigate the localization of ROVsusing the cable that connects it to the surface, without the need for additional equipment on site. If known, the shape of the umbilical cable can determine the position of the ROV at its end point. Several works address the problem of cable shape estimation for tethered robotic system, in terrestrial, aerial and underwater applications. Some cables are designed in order to estimate their shape directly, by the use of proprioceptive sensors. The deformation of optical fiber cables can be measured by reflectometry techniques [12], [13], [14]. Other works consider IMUs placed all along a cable and deduce its shape from IMU measurements integration [15]. However, these technologies require specific expensive cables or cable instrumentation, which are not the standard in marine robotics. Alternatively, the shape of a cable can be estimated according to a physical or geometrical model. Lumped-mass-spring [16], [17], [18] or finite-elements [19], [20], [21] methods can provide a dynamic model of the cable given the forces applied to it, but these methods require a significant amount of computational resources and time and strongly depend on the knowledge of the physical parameters of the system. Alternatively, simpler geometrical models can be used. One of them is the catenary model [22], [23], [24], [25], which gives the shape of a quasi-static, non-neutrally buoyant, hanging cable as a parametric three-dimensional curve. The catenary parameters can be computed from visual observation [22] or cable tangent inertial measurements at one or two points [24]. However, this model is only valid if the cable weight or buoyancy is very predominant with respect to the other external and internal forces exerted on the cable [24], [25]. It is therefore not suitable in the presence of currents, for cable with neutral or close-to-neutral buoyancy, or if cable stiffness is too high.

Other tethered systems constrain the cable to a piecewise linear model [26], [27], [28]. In [26], a piecewise linear shape is deduced from cable angle and tension measurement and entanglements in a terrestrial cluttered environment. In [27], [28], the cable of a ROV is equipped with a system of ballasts and buoys which stretches the tether to conform it into a simple predictable shape, assimilated to straight lines. In [1], the authors present a method to estimate the position of the ROV from this umbilical model using local angles and depth. This method was validated in a pool, using a gold standard measure of the model parameters from an underwater motion capture system that tracked the cable and the ROV. Because underwater motion capture tracking is not available outdoors and in field, the measurement of model parameters from embedded sensors was discussed, and was subject to a preliminary feasibility test, as a proof of concept.

The present work extends the concept exposed in [1] to propose a real implementation of the method using embedded sensors to measure parameters, and a more complete model of the umbilical considering the presence of curves at the vicinity of the siding element. The orientation angles of the stretched parts are measured by two watertight IMUs mounted on the cable. The depth of cable ends is given by an embedded pressure sensor. The current approach does not require motorization or a mechanical tether management system, and does not depend on a motion capture system for angle reading. Two cable configurations are studied. In the first configuration, the umbilical connects the ROV directly to a point at the surface. In the second configuration the cable connects a ROV to another one, and corresponds to the use of

intermediary ROVs in cable management strategies, namely ROV chains [22], [24].

III. System modeling

Figure 1 represents a scheme of the system. Cable attachment point on the ROV is denoted $\mathbf{E}$, and the other attachment point is denoted $\mathbf{O}$. The first part of the cable from $\mathbf{O}$ is constrained to be vertical down by a fixed anchor placed in $\mathbf{A}$, and a sliding ballast is placed along the cable between $\mathbf{A}$ and $\mathbf{E}$. Note that one can take $\mathbf{O} = \mathbf{A}$. The sliding ballast is composed of a mass fixed on a pulley, which can slide freeely along the cable. A cartesian reference frame $\mathcal{F}_\mathbf{O} = (\mathbf{O}, \mathbf{x_O}, \mathbf{y_O}, \mathbf{z_O})$ is defined with its z-axis vertical, downwards.

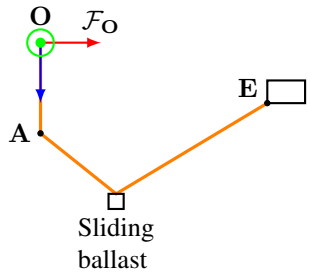

Fig. 1. System overview. Red, green and blue axis represent the x, y and z-axis of $\mathcal{F}_\mathbf{O}$ respectively.

Note that a similar system can be defined by replacing the sliding ballast by a sliding buoy, even though the current work focuses on the ballast configuration. To this end, we introduce the buoyancy parameter s_b such that $s_b = 1$ if the sliding element is a ballast and $s_b = -1$ if it is a buoy.

A. Assumptions ans application scope

The following assumptions are considered:

(A1) The ratio of mass to buoyancy of the umbilical is negligible compared to the ballast's weight, or currents applied to the ballast;

(A2) The length variation of the umbilical is negligible compared to its length, which is therefore considered constant;

(A3) When the umbilical is taut, its geometry can be assimilated to straight lines between defined points, here the ballast and the endpoints of the umbilical;

(A4) The umbilical attachment point $\mathbf{O}$ and the optional anchor point $\mathbf{A}$ are assumed to be strong or heavy enough to be unaffected by the action of the umbilical and the ROV, and so can be considered motionless;

(A5) ROV motion and cable length are such that the umbilical remains taut. Constraints to meet this assumption are discussed in [28].

The validity of these assumptions will be discussed further in the experimental part, in Section V. The application scope of the present system is for ROVs having an umbilical shorter than 50 m, in order to ensure assumptions **(A1)** and **(A2)**. In addition, to respect assumption **(A3)**, the current system requires the umbilical to be flexible and allow the sliding ballast to move freely along it. Therefore, the current method is suitable for the following scenarios:

- Exploration of shallow water from a boat with a depth of less than 50m, with zero or stable currents,
- Ship's hull inspection, navigation under uniform ice, etc., since the sliding ballast must remain submerged without touching any obstacle or the sea floor to keep the cable taut,
- Umbilical between an ROV and its cage in case of deep exploration. The umbilical length is then measured from the cage, which is is considered as an anchor in this study. The cable between the boat and the cage, then, does not need to meet the assumptions described above.
- Chain of ROVs connected with the same umbilical, the model being applicable for each section of cable linking two consecutive ROVs.

B. Cable model

Let us consider a system composed of a ROV tethered to a point $\mathbf{O}$ by an umbilical of length l, as described below. Let us model the pulley of the sliding ballast by a circle $\mathcal{C}$ of center $\mathbf{C}$ and radius r. Let us define $\mathbf{B}_1$ and $\mathbf{B}_2$ the points where the first and last contact between the cable and the pulley are located. The umbilical is then divided in four parts (Fig. 2):

1) the linear part $l_0 = \|\mathbf{OA}\|$ between attachment point $\mathbf{O}$ and an anchor $\mathbf{A}$
2) the linear part $l_{c_1} = \|\mathbf{AB}_1\|$ between the anchor $\mathbf{A}$ and the first contact between the cable and the pulley in $\mathbf{B}_1$
3) the arc made by the pulley $l_p = \overset{\frown}{\mathbf{B}_1\mathbf{B}_2}$
4) the linear part $l_{c_2} = \|\mathbf{B}_2\mathbf{E}\|$ between the last contact between the cable and the pulley in $\mathbf{B}_2$ and the ROV $\mathbf{E}$.

Let L_c denote the length of the cable between the anchor $\mathbf{A}$ and the ROV $\mathbf{E}$ such that $L_c = l_{c_1} + l_p + l_{c_2}$, where L_c is fixed. The sliding ballast can move freely on the cable L_c. In addition, the cable length l is such that $l = l_0 + L_c$. Note that $l_0 = 0$ if the anchor $\mathbf{A} = \mathbf{O}$, and then one gets $l = L_c$.

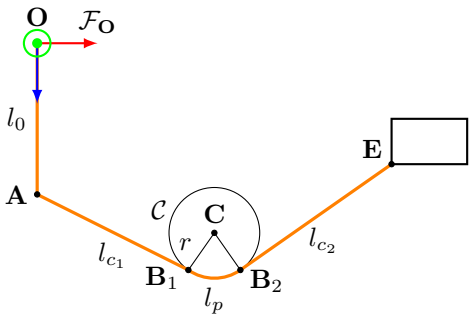

Fig. 2. System model including the pulley of center $\mathbf{C}$. The mass attached to the pulley is not represented.

Let us denote $\mathbf{B}$ the intersection of lines $\mathbf{AB}_1$ and $\mathbf{B}_2\mathbf{E}$

(see Figure 3). In addition, let us define the following lengths:

$$l_{p_1} = \|\mathbf{B}_1\mathbf{B}\| \tag{1}$$
$$l_{p_2} = \|\mathbf{B}\mathbf{B}_2\| \tag{2}$$
$$l_1 = \|\mathbf{A}\mathbf{B}\| = l_{c_1} + l_{p_1} \tag{3}$$
$$l_2 = \|\mathbf{B}\mathbf{E}\| = l_{c_2} + l_{p_2} \tag{4}$$
$$\hat{L} = l_1 + l_2 \tag{5}$$
$$\tag{6}$$

and non-oriented angles:

$$\sigma = \widehat{\mathbf{B}_1\mathbf{B}\mathbf{C}} \tag{7}$$
$$\psi = \widehat{\mathbf{B}_2\mathbf{B}\mathbf{C}} \tag{8}$$
$$\theta = \sigma + \psi \tag{9}$$

System parameterization at the vicinity of the pulley is represented in Figure 3.

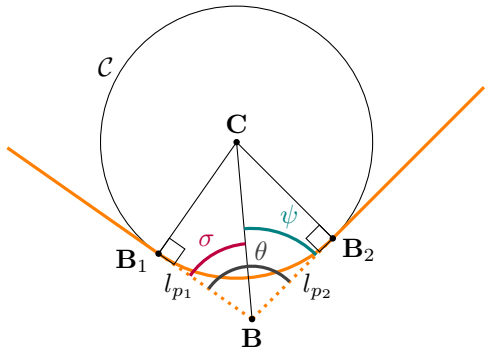

Fig. 3. Cable shape parameterization at the position of the pulley.

Following the steps described in Appendix A, parameters $\hat{L}$, l_{p_1} and l_{p_2} can be expressed from pulley radius r and angle $\theta = \sigma + \psi$ by

$$l_{p1} = l_{p2} \tag{10}$$
$$= \tan\left(\frac{\pi - \theta}{2}\right) r \tag{11}$$
$$\hat{L} = L_c - r\,(\pi - \theta) + 2\tan\left(\frac{\pi - \theta}{2}\right) r \tag{12}$$

Note that $\lim_{\theta \to 0} \hat{L}(\theta, r) = +\infty$, *i.e.* when cable segments $\mathbf{AB}_1$ and $\mathbf{B}_2\mathbf{E}$ become parallel. A saturation can so be added such that if $\hat{L} > L_{max}$ for a defined L_{max}, one keeps $\hat{L} = L_c$.

If the pulley is very small, the length $\hat{L}$ can be simplified to $\hat{L} = L_c$ by neglecting the cable deformation caused by the pulley. The validity and influence of the model of the pulley described in the current section will be discussed in Section V.

Let us define angles α, β, μ and η as follows:

- α is the angle between the z-axis of $\mathcal{F}_\mathbf{O}$ and segment $\mathbf{AB}$ around the y-axis of $\mathcal{F}_\mathbf{O}$, in plane $(\mathbf{O}, \mathbf{x_O}, \mathbf{z_O})$;
- β is the angle between segment $\mathbf{BE}$ and the z-axis of $\mathcal{F}_\mathbf{O}$ around the y-axis of $\mathcal{F}_\mathbf{O}$, in plane $(\mathbf{O}, \mathbf{x_O}, \mathbf{z_O})$;
- μ is the angle between segment $\mathbf{AB}$ and the z-axis of $\mathcal{F}_\mathbf{O}$ around the x-axis of $\mathcal{F}_\mathbf{O}$, in plane $(\mathbf{O}, \mathbf{y_O}, \mathbf{z_O})$;
- η is the angle between the z-axis of $\mathcal{F}_\mathbf{O}$ and segment $\mathbf{BE}$ around the x-axis of $\mathcal{F}_\mathbf{O}$, in plane $(\mathbf{O}, \mathbf{y_O}, \mathbf{z_O})$.

These angles are represented in Figure 4. In addition, we define l_{1_x} and l_{1_y} as the lengths of the projected vector $\mathbf{AB}$ on planes $(\mathbf{O}, \mathbf{x_O}, \mathbf{z_O})$ and $(\mathbf{O}, \mathbf{y_O}, \mathbf{z_O})$ respectively. l_{2_x} and l_{2_y} are defined similarly for vector $\mathbf{BE}$.

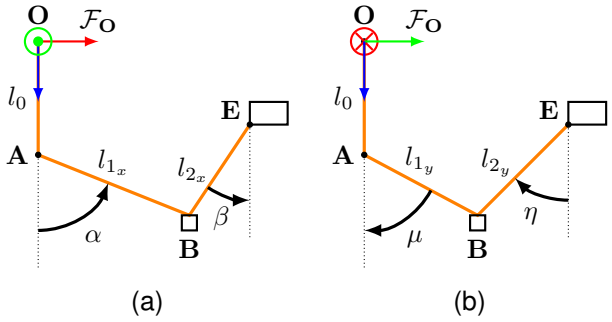

Fig. 4. Angle parametrization of the system in planes $(\mathbf{O}, \mathbf{x_O}, \mathbf{z_O})$ (4a) and $(\mathbf{O}, \mathbf{y_O}, \mathbf{z_O})$ (4b)

Let ${}^\mathbf{O}\mathbf{E} = \begin{bmatrix} {}^\mathbf{O}x_\mathbf{E} & {}^\mathbf{O}y_\mathbf{E} & {}^\mathbf{O}z_\mathbf{E} \end{bmatrix}^T$ denote the coordinates of $\mathbf{E}$ in frame $\mathcal{F}_\mathbf{O}$. As demonstrated in Appendix B and C, ${}^\mathbf{O}x_\mathbf{E}$ and ${}^\mathbf{O}y_\mathbf{E}$ can be expressed as

$$\begin{cases} {}^\mathbf{O}x_\mathbf{E} = & l_{1x}\sin(\alpha) + l_{2x}\sin(\beta) \\ {}^\mathbf{O}y_\mathbf{E} = & l_{1y}\sin(\mu) + l_{2y}\sin(\eta) \end{cases} \tag{13}$$

where

$$l_{1_x} = \frac{l_1}{\sqrt{1 + \tan(\mu)^2\cos(\alpha)^2}} \tag{14}$$
$$l_{1_y} = \frac{l_1}{\sqrt{\sin(\mu)^2 + \left(\frac{\cos(\mu)}{\cos(\alpha)}\right)^2}} \tag{15}$$
$$l_{2_x} = \frac{l_2}{\sqrt{1 + \tan(\eta)^2\cos(\beta)^2}} \tag{16}$$
$$l_{2_y} = \frac{l_2}{\sqrt{\sin(\eta)^2 + \left(\frac{\cos(\eta)}{\cos(\beta)}\right)^2}} \tag{17}$$

and l_1 and l_2 can be expressed as a function of $\hat{L}$, ${}^\mathbf{O}z_\mathbf{E}$, α, β, μ and η as follows:

$$l_1 = \hat{L} - l_2 \tag{18}$$
$$l_2 = \frac{\left(\frac{\hat{L}\cos(\alpha)}{a_1} - s_b\left({}^\mathbf{O}z_\mathbf{E} - l_0\right)\right)}{\left(\frac{\cos(\alpha)}{a_1} + \frac{\cos(\beta)}{a_2}\right)} \tag{19}$$

where

$$a_1 = \sqrt{1 + \tan(\mu)^2\cos(\alpha)^2} \tag{20}$$

and

$$a_2 = \sqrt{1 + \tan(\eta)^2\cos(\beta)^2} \tag{21}$$

From (12), $\hat{L}$ is a function of θ. As shown in Appendix D, θ can be deduced from angles α, β, μ and η as follows:

$$\theta = \arccos\left(\frac{\cos(\alpha+\beta)}{a_1 a_2} - \frac{\sin(\mu)\sin(\eta)}{a_3 a_4}\right) \tag{22}$$

where a_1 and a_2 are defined in (20) and (21), and:

$$a_3 = \sqrt{\sin(\mu)^2 + \left(\frac{\cos(\mu)}{\cos(\alpha)}\right)^2} \tag{23}$$

$$a_4 = \sqrt{\sin(\eta)^2 + \left(\frac{\cos(\eta)}{\cos(\beta)}\right)^2} \tag{24}$$

${}^{\mathbf{O}}x_{\mathbf{E}}$ and ${}^{\mathbf{O}}y_{\mathbf{E}}$ can therefore be deduced from variable parameters ${}^{\mathbf{O}}z_{\mathbf{E}}$, α, β, μ and η, and constant parameters L_c, r, l_0 and s_b, where is $s_b = 1$ in the current case since the sliding element is a ballast. Finally, estimation of the coordinates of $\mathbf{E}$ in $\mathcal{F}_{\mathbf{O}}$ allows estimating the position of the ROV by locating the cable attachment $\mathbf{E}$ on the ROV with respect to the other cable attachment point $\mathbf{O}$ used as a reference. In the following, $\mathbf{E}$ is equally referred to as 'ROV position' and 'cable attachment point on the ROV.

It is worth noticing that, unlike [27], the current study does not require the knowledge of the forces of the ballast, buoyancy, nor current to estimate the position of the ROV. Indeed, these forces are automatically considered in the models with the orientation and value of the angles.

C. Parameters constraints

The sliding ballast must not enter in collision with an obstacle, the seafloor or the surface, what constrains the minimum depth allowed for the ROV. Let ${}^{\mathbf{O}}z_{\text{floor}}$ be the minimum z-coordinate in $\mathcal{F}_{\mathbf{O}}$ of the seabed or of a submarine obstacle inside the sphere of center $\mathbf{A}$ and radius L, which delimits the area in which the ROV can move. First, the anchor must respect the constraint

$$l_0 \leq {}^{\mathbf{O}}z_{\text{floor}} \tag{25}$$

to not touch the seafloor, and so the ballast when it is in contact with the anchor. Then, the ballast will never touch the seafloor if

$$l_0 + L_c \leq {}^{\mathbf{O}}z_{\text{floor}} \tag{26}$$

This condition can be relaxed if the z-coordinate ${}^{\mathbf{O}}z_{\mathbf{E}}$ of the ROV in $\mathcal{F}_{\mathbf{O}}$ respects

$${}^{\mathbf{O}}z_{\mathbf{E}} < {}^{\mathbf{O}}z_{\text{lim}} \tag{27}$$

where ${}^{\mathbf{O}}z_{\text{lim}}$ depends on the ROV's x and y-coordinates in $\mathcal{F}_{\mathbf{O}}$. It has been demonstrated in previous work [27] that an acceptable value for ${}^{\mathbf{O}}z_{\text{lim}}$ is

$${}^{\mathbf{O}}z_{\text{lim}} = 2\left({}^{\mathbf{O}}z_{\text{floor}} - h_B\right) - \hat{L}\sqrt{1 - \left(\frac{{}^{\mathbf{O}}x_{\mathbf{E}}{}^2 + {}^{\mathbf{O}}y_{\mathbf{E}}{}^2}{\hat{L}^2}\right)} \tag{28}$$

where h_B denotes the height of the sliding element. (28) can be simplified by:

$${}^{\mathbf{O}}z_{\text{lim}} = 2\left({}^{\mathbf{O}}z_{\text{floor}} - h_B\right) - L_c\sqrt{1 - \left(\frac{{}^{\mathbf{O}}x_{\mathbf{E}}{}^2 + {}^{\mathbf{O}}y_{\mathbf{E}}{}^2}{L_c^2}\right)} \tag{29}$$

since $L_c \approx \hat{L}$ with $L_c < \hat{L}$. The interest of using L_c instead of $\hat{L}$ is that this value is known precisely and is constant.

IV. Parameters measurement

Section III-B gave the position $\mathbf{E}$ of the ROV from constant, calibrated parameters and from the set of variable parameters ${}^{\mathbf{O}}z_{\mathbf{E}}$, α, β, μ and η which need to be measured using embedded sensors. The embedded sensors include an IMU and a water pressure sensor for the ROV and two IMUs positioned along the cable, on segments $\mathbf{AB}$ and $\mathbf{EB}$ respectively.

A. Measurement of ${}^{\mathbf{O}}z_{\mathbf{E}}$

${}^{\mathbf{O}}z_{\mathbf{E}}$ is the difference of depth between the cable attachment points $\mathbf{O}$ and $\mathbf{E}$, of respective depth $d_{\mathbf{O}}$ and $d_{\mathbf{E}}$:

$${}^{\mathbf{O}}z_{\mathbf{E}} = d_{\mathbf{E}} - d_{\mathbf{O}} \tag{30}$$

Depth $d_{\mathbf{E}}$ is measured using the ROV's water pressure sensor and IMU. The pressure sensor is located in $\mathbf{D}$. The IMU is placed in $\mathbf{I}_r$ and gives the orientation of the inertial frame $\mathcal{F}_{\mathbf{I}_r}$ with respect to a world frame $\mathcal{F}_w$ with its z-axis vertical, upwards. This orientation is represented by a rotation matrix ${}^{w}\mathbf{R}_{\mathbf{I}_r}$. The system is represented in Figure 5. Let us define frame $\mathcal{F}_{\mathbf{D}}$ with origin $\mathbf{D}$ and same orientation as $\mathcal{F}_{\mathbf{I}_r}$. The position ${}^{\mathbf{D}}\mathbf{E}$ of point $\mathbf{E}$ in $\mathcal{F}_{\mathbf{D}}$ is fixed and is assumed to be calibrated.

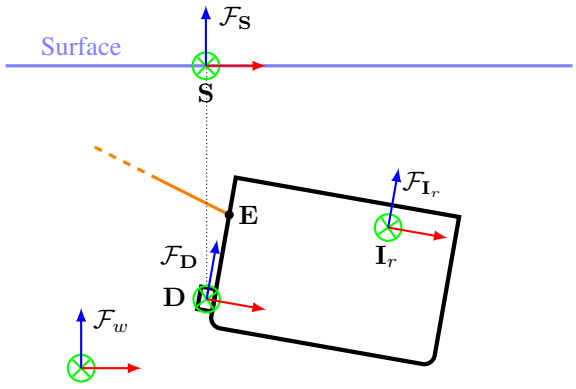

Fig. 5. Points and frames involved in the computation of $d_{\mathbf{E}}$

As demonstrated in Appendix E,

$$d_{\mathbf{E}} = -\begin{bmatrix}0 & 0 & 1 & 0\end{bmatrix} {}^{\mathbf{S}}\mathbf{T}_{\mathbf{D}}\, {}^{\mathbf{D}}\overline{\mathbf{E}} \tag{31}$$

where ${}^{\mathbf{D}}\overline{\mathbf{E}}$ is the position of $\mathbf{E}$ in $\mathcal{F}_{\mathbf{D}}$ in homogeneous coordinates and where ${}^{\mathbf{S}}\mathbf{T}_{\mathbf{D}}$ is a rigid transformation matrix defined from the rotation matrix ${}^{w}\mathbf{R}_{\mathbf{I}_r}$ and the depth at the position of the water pressure sensor $d_{\mathbf{D}}$ by the relation:

$${}^{\mathbf{S}}\mathbf{T}_{\mathbf{D}} = \left[\begin{array}{c|c} {}^{w}\mathbf{R}_{\mathbf{I}_r} & \begin{matrix}0\\0\\d_{\mathbf{D}}\\1\end{matrix} \end{array}\right] \tag{32}$$

The depth $d_{\mathbf{D}}$ is deduced from the water pressure measurement $P_{\mathbf{D}}$ in $\mathbf{D}$ by the relation

$$d_{\mathbf{D}} = \frac{P_{\mathbf{D}} - P_0}{\rho_{\text{water}} * g} \tag{33}$$

where ρ_{water} is water density of water, g is the value of Earth gravity and P_0, is the pressure returned by the pressure sensor at zero depth.

If $\mathbf{O}$ is a fixed point, $d_{\mathbf{O}}$ can be calibrated. Otherwise, for instance if $\mathbf{O}$ is placed on a second ROV, $d_{\mathbf{O}}$ can be measured similarly to $d_{\mathbf{E}}$.

B. Measurement of angles α, β, μ and η

Angles (α, μ) and (β, η) are measured pairwise by two IMUs placed along the cable. As represented in Figure 6, IMUs indexed 1 and 2 are positioned on segments $\mathbf{AB}$ and $\mathbf{EB}$ in $\mathbf{I}_1$ and $\mathbf{I}_2$ respectively such that IMU j, $j \in \{1, 2\}$ is tangent to the cable along unit vector $\mathbf{v}_{i_j}$.

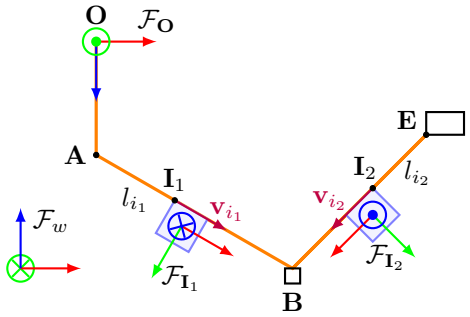

Fig. 6. Points and frames involved in the computation of α, β, μ and η

Each IMU j measures the orientation of its inertial frame $\mathcal{F}_{\mathbf{I}_j}$ with respect to the world reference frame $\mathcal{F}_w$ as introduced in Section IV-A, with z-axis vertical, upwards. The coordinates ${}^{\mathbf{I}_j}\mathbf{v}_{i_j}$ of each vector $\mathbf{v}_{i_j}$ in $\mathcal{F}_{\mathbf{I}_j}$ are fixed and assumed to be calibrated. In addition, let us define the lengths

$$l_{i_1} = \|\mathbf{AI}_1\| \tag{34}$$
$$l_{i_2} = \|\mathbf{EI}_2\| \tag{35}$$

$\forall j \in \{1, 2\}$, the coordinates ${}^{\mathbf{O}}\mathbf{v}_{i_j}$ can be expressed as

$${}^{\mathbf{O}}\mathbf{v}_{i_j} = {}^{\mathbf{O}}\mathbf{R}_w \, {}^{w}\mathbf{R}_{\mathbf{I}_j} \tag{36}$$

where the rotation matrix ${}^{w}\mathbf{R}_{\mathbf{I}_j}$ is given by the measurements of IMU j and ${}^{\mathbf{O}}\mathbf{R}_w$ is the rotation matrix between frames $\mathcal{F}_w$ and $\mathcal{F}_{\mathbf{O}}$. Because the choice of the orientation of $\mathcal{F}_{\mathbf{O}}$ is arbitrary except from it z-axis being vertical, downwards, $\mathcal{F}_{\mathbf{O}}$ can be selected such that ${}^{\mathbf{O}}\mathbf{R}_w$ is constant and calibrated, or variable but measured, for instance using an additional IMU.

Finally, angles α and μ can be deduced from ${}^{\mathbf{O}}\mathbf{v}_{i_1}$ by the relations

$$\alpha = \text{angle}((\mathbf{I}_3 - \mathbf{y}\mathbf{y}^T){}^{\mathbf{O}}\mathbf{v}_{i_1}, \mathbf{z}) \tag{37}$$
$$\mu = \text{angle}((\mathbf{I}_3 - \mathbf{x}\mathbf{x}^T){}^{\mathbf{O}}\mathbf{v}_{i_1}, \mathbf{z}) \tag{38}$$

where $\mathbf{I}_3$ is the 3×3 identity matrix and

$$\mathbf{x} = \begin{bmatrix} 1 & 0 & 0 \end{bmatrix}^T \tag{39}$$
$$\mathbf{y} = \begin{bmatrix} 0 & 1 & 0 \end{bmatrix}^T \tag{40}$$
$$\mathbf{z} = \begin{bmatrix} 0 & 0 & 1 \end{bmatrix}^T \tag{41}$$

Similarly, β and η can be obtained from ${}^{\mathbf{O}}\mathbf{v}_{i_2}$ by:

$$\beta = \text{angle}((\mathbf{I}_3 - \mathbf{y}\mathbf{y}^T){}^{\mathbf{O}}\mathbf{v}_{i_2}, \mathbf{z}) \tag{42}$$
$$\eta = \text{angle}((\mathbf{I}_3 - \mathbf{x}\mathbf{x}^T){}^{\mathbf{O}}\mathbf{v}_{i_2}, \mathbf{z}) \tag{43}$$

V. Experiments

Experiments are conducted in pools in order the validate the proposed ROV localization system[1]. Two configurations are studied, including a ROV tethered to a fixed point and a pair of ROVs connected together by a cable (ROV chain). The influence of the position of the IMUs along the cable on ROV localization accuracy is also studied, as well as the influence of model parameters measurement errors and the influence of including the effect of the pulley in the cable model.

A. System

1) Pools: Two different pools have been used for the experiments, denoted *indoor pool* and *outdoor pool* respectively. Their dimensions are given in Table I. The cable length used for the experiments was therefore restricted by the dimensions of the pools.

TABLE I
Pool dimensions

Pool	*Indoor pool*	*Outdoor pool*
Depth (m)	3	6
Length (m)	7.2	15
Width (m)	4.2	10

The *indoor pool* is made of steel and the *outdoor pool* contains big steel parts, what prevents the use of magnetometer data in these pools, leading to IMU yaw drift.

2) Robotic system: The experiments use the BlueROV2[2] from BlueRobotics, which embeds an IMU, a water pressure sensor and a camera. The cable is equipped with a pair of PhidgetSpatial Precision 3/3/3 High Resolution IMUs[3] sealed in waterproof housings. The sliding ballast is composed of a neutrally buoyant pulley holding a 240 g lead mass, with a pulley radius $r = 2.175$ cm. The sliding ballast and the cable IMUs are pictured in Figure 7.

IMUs measurements are integrated using a Madgwick filter [29] in order to compute IMU orientation. In the absence of magnetometer data because of the large steel-made parts in the pools, the IMU yaw drift is approximated as linear and calibrated on a static sequence in order to be corrected from the measurements. The standard deviation on the resulting orientation measurements is evaluated on a static sequence

[1] Video available at https://www.youtube.com/channel/UCi8aAbpu8Hjxw3wBXuQfkHw
[2] https://bluerobotics.com/store/rov/bluerov2/
[3] https://www.phidgets.com/?prodid=32

Fig. 7. Cable IMU in waterproof housing (7a) and 240 g sliding ballast (7b)

TABLE II
IMU ERRORS ON ORIENTATION MEASUREMENT

	IMU 1	IMU 2
yaw drift ($°/s$)	0.628	-0.599
σ_y ($°$)	0.334	0.041
σ_p ($°$)	0.158	0.330
σ_r ($°$)	0.621	0.582

with respect to Euler angles. These values are given in Table II. The orientation is expressed in Euler angles using the convention:

$$\mathbf{R} = \mathbf{R}_z(\theta_y)\,\mathbf{R}_y(\theta_p)\,\mathbf{R}_x(\theta_r) \tag{44}$$

with yaw θ_y, pitch θ_p and roll θ_r. σ_r, σ_p and σ_y are the standard deviation of the angle measurement, for the roll, pitch and yaw after drift correction respectively.

B. ROV connected to a fixed point

A first experiment is set-up in the *indoor pool*, featuring a BlueROV tethered to a fixed point by its Fathom Slim communication cable[4] such that $l_0 = 0$ m and $L = 3$ m. Cable IMUs are placed such that $l_{i_1} = 0.4$ m and $l_{i_2} = 0.2$ m. These positions are selected arbitrarily to be far enough from the cable ends to make sure angle measurement is not disturbed by the cable's stiffness, but also close enough from the ends not to block the displacement of the sliding ballast. A 5-cameras Qualisys underwater motion capture (mocap) system[5] is set up in the pool in order to track the three-dimensional system. To this end, the robot, the sliding ballast and the cable are equipped with reflective spherical markers. Cable markers are made by reflective tape stuck around the cable every 20 cm. Tape pieces are thin enough not to affect the movements of the sliding ballast. Markers tracking accuracy is about 1 cm. Motion capture output is used as a reference for evaluating the accuracy of the ROV localization system introduced in the current paper. The system is pictured in Figure 8.

The *IMU-based* ROV localization described in the current paper is compared with the *ground truth* ROV location provided by the mocap system, but also to the location

[4]https://bluerov-solutions.com/produkt/fathom-slim-rov-tether-rov-ready/
[5]https://www.qualisys.com/cameras/underwater/

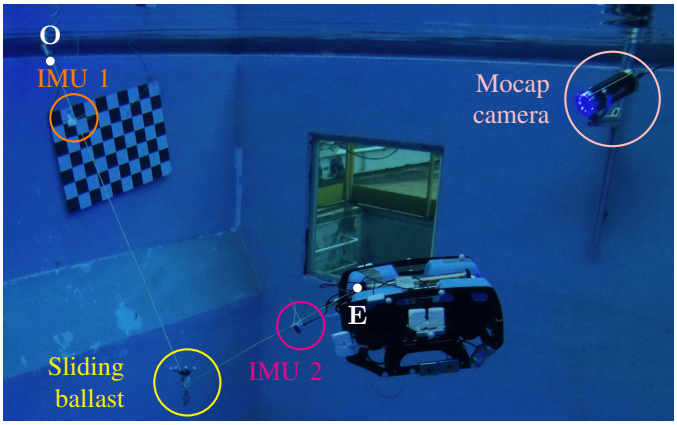

Fig. 8. Experimental system. Reflective markers are placed on the robot, the pulley, and along the cable.

computed using mocap measurements of parameters ${}^{\mathbf{O}}z_{\mathbf{E}}$, α, β, μ and η, like in [1]. This last estimation is referred to as *mocap-based*. IMU and mocap measurements are put in the same referential frame $\mathcal{F}_{\mathbf{O}}$ by a change of coordinate frame, for comparison purpose. The data is processed offline, including a synchronization of clock between the IMU and mocap measurements, as well as the transformation between mocap and sensor frames. Two motion sequences are recorded, indexed 1 and 2. Sequence 1 is a short sequence featuring very slow displacements with small range, while Sequences 2 is a four-minutes sequence showing ROV displacements closer to a real use case, with higher speed, motion variation and displacement range. ROV localization results and error with respect to mocap *ground-truth* are represented in Figures 9 and 10 for Sequences 1 and 2 respectively. The error e is the distance between the ground truth and the estimated ROV position.

One can see that the results of *IMU-based* ROV localization are particularly close to the *ground truth* in Sequence 1, with an error of about 0.15 m only. *IMU-based* ROV localization shows a slightly lower accuracy but the corresponding results are still very close to those of the *mocap-based* ROV localization, meaning that the cable angles are estimated very accurately by the IMUs. This result shows that the proposed localization method can lead to a very accurate ROV position estimation if the ROV is close to stationary. ROV localization error is higher for Sequences 2. The error is about 0.20 m for the *IMU-based* approach, which is thus acceptable for the tested configuration. The *mocap-based* approach results in a 0.02 m error, showing that the accuracy of the method is directly proportional to the accuracy of the angle measurement. These results demonstrate the validity of the theoretical model and the possibility of obtaining a fairly accurate position even when the ROV is in motion, since the umbilical remains stretched by the ballast during the displacement.

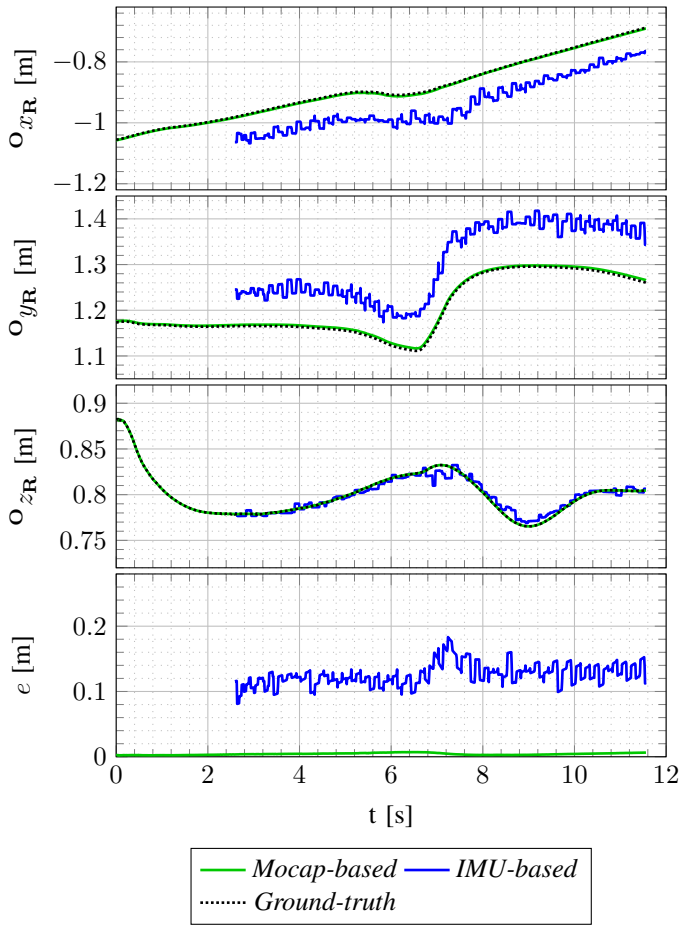

Fig. 9. *IMU-based*, *mocap-based* and *ground truth* ROV position and positioning error for Sequence 1 ($[l_{i_1}, l_{i_2}]$ = [0.20,0.40] m). The starting and ending timestamps of the curves differ because the mocap system and sensor recording were not monitored to be simultaneous. Note that the *mocap-based* and *ground truth* curves overlap very closely.

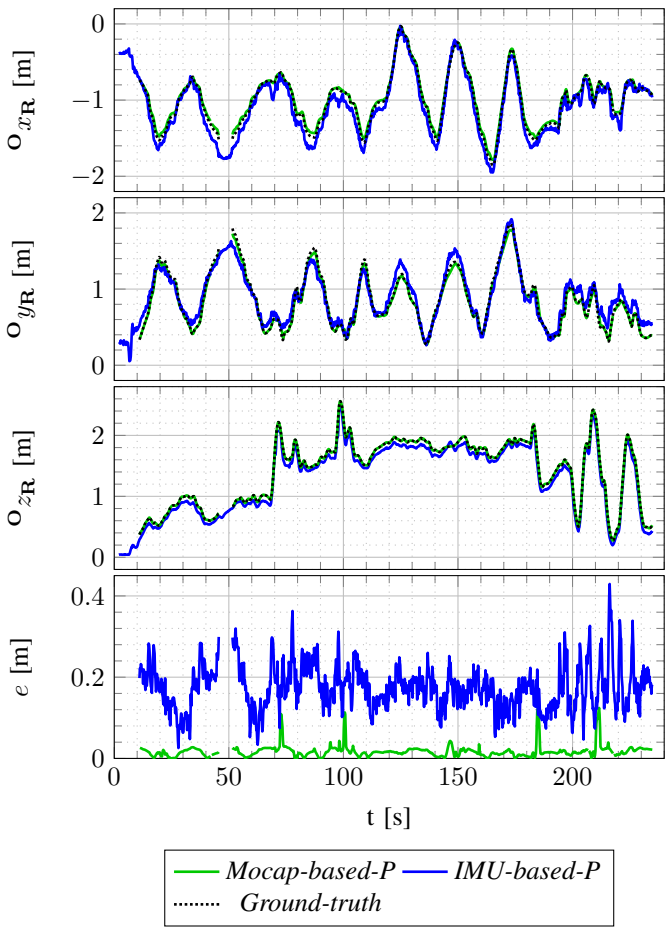

Fig. 10. *IMU-based*, *mocap-based* and *ground truth* ROV position and positioning error for Sequence 2 ($[l_{i_1}, l_{i_2}]$ = [0.20,0.40] m). Gaps in the curves computed from the mocap recording are caused by a few system tracking failures. Gaps in the *IMU-based* estimation are caused by temporary inconsistent measurements from which no localization could be computed.

C. Influence of IMU positioning

Due to the stiffness of the cable, local cable orientation may vary slightly along the cable and be more or less representative of the global cable segment orientation. The influence of the positions of the IMUs along the cable is therefore examined by reproducing the experiment described in Section V-B with different values of l_{i_1} and l_{i_2}. Two positions are compared for each IMU, with l_{i_1} = 0.40 m or 0.78 m and l_{i_2} = 0.20 m or 0.40 m, resulting in four distinct $\{l_{i_1}, l_{i_2}\}$ configurations. Sequences 1 and 2 studied in Section V-B feature the $\{l_{i_1} = 0.40 \text{ m}, l_{i_2} = 0.20 \text{ m}\}$ configuration. Three additional sequences indexed from 3 to 5 are recorded in order to test the three remaining $\{l_{i_1}, l_{i_2}\}$ configurations. Similarly to Sequence 2, Sequences 3, 4 and 5 involve motion close to a real ROV use case, with speed and motion variations and large displacement range.

The resulting ROV localization results and error with respect to mocap *ground-truth* are represented in Figures 11, 12 and 13. The mean, median and standard deviation (σ) of ROV position error for each $\{l_{i_1}, l_{i_2}\}$ configuration are reported in Table III, based on Sequences 2, 3, 4 and 5, where the lowest and highest values for each criterion are highlighed in green and red respectively. Because Sequence 1 is the only quasi-static sequence, it is omitted from this analysis.

TABLE III
STATISTICS ON ROV POSITION ERROR e FOR EACH $\{l_{i_1}, l_{i_2}\}$ CONFIGURATION FOR *IMU-based* ESTIMATION. THE LOWEST AND HIGHEST VALUES FOR EACH CRITERIA ARE HIGHLIGHTED IN GREEN AND RED RESPECTIVELY.

Sequence	#2	#3	#4	#5
l_{i_1} (m)	0.40	0.78	0.78	0.40
l_{i_2} (m)	0.20	0.20	0.40	0.40
mean (m)	**0.175**	0.179	0.178	**0.191**
median (m)	0.172	0.175	**0.159**	**0.196**
σ (m)	**0.057**	**0.090**	0.089	0.064

One can observe that the position of the IMUs appears to have little to no impact on the results. Indeed, all configurations lead to the same error order of magnitude, between 0.15 m and 0.20 m. These results show that the *IMU-based* method proposed in the current work is therefore

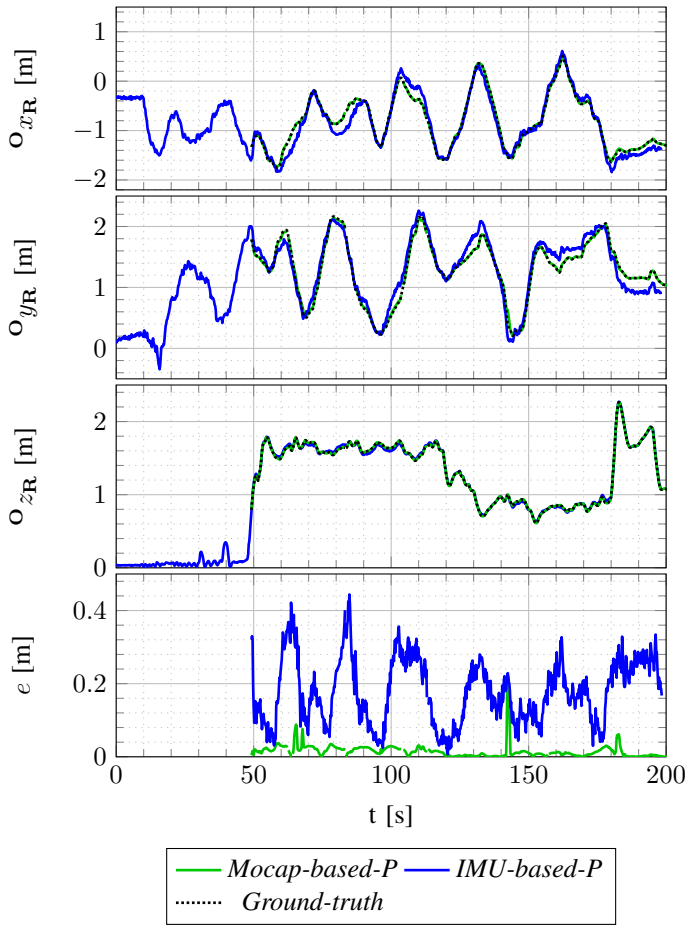

Fig. 11. *IMU-based*, *mocap-based* and *ground truth* ROV position and positioning error for Sequence 3 ($[l_{i_1}, l_{i_2}] = [0.78, 0.20]$ m).

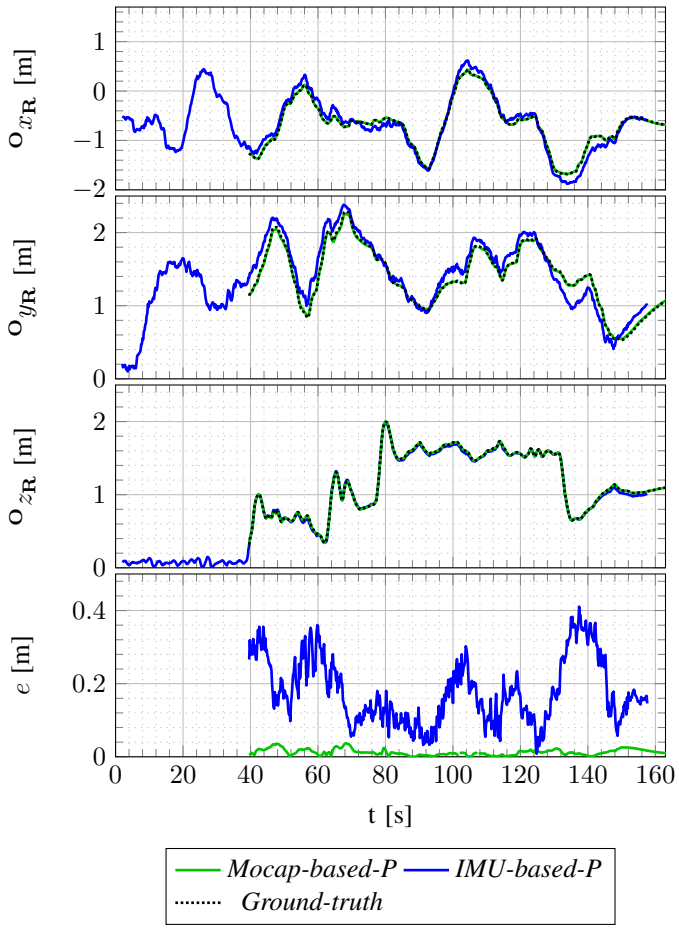

Fig. 12. *IMU-based*, *mocap-based* and *ground truth* ROV position and positioning error for Sequence 4 ($[l_{i_1}, l_{i_2}] = [0.78, 0.40]$ m).

flexible with respect to the installation of IMUs on the umbilical, whose position can be chosen so as to obstruct the *sliding ballast* as little as possible.

D. ROV chain

A second system is studied, featuring a pair of BlueROVs connected together by a cable equipped with a sliding ballast, and therefore forming a robot chain. The connection cable between the robots is simulated by a 3 m long cord. This system is deployed in the *outdoor pool*. The main advantage of this pool compared to the *indoor pool* used in Sections V-B and V-C is that it is larger and deeper, making it easier to deploy a two-robot system. However, it is not compatible with the underwater mocap system used in Sections V-B and V-C, which does not work outdoors. Instead, we take advantage of the embedded cameras of the ROVs to generate a Structure from Motion (SfM) localization baseline. This baseline is assumed to be far less precise than the mocap ground truth used in the previous sequences because of the accuracy of the SfM itself, but also and mostly because transferring the SfM estimated pose to the attachment points involve calibrations which introduce important sources of imprecision. However, an accuracy of a few centimeters is to be expected, making this SfM baseline still suitable for evaluating our cable-based ROV localization method.

The system is represented in Figure 14, and pictured in Figure 15. $\forall\, k \in \{1, 2\}$, Robot k embeds an IMU in $\mathbf{P}_{i_{r,k}}$, a camera in $\mathbf{P}_{c_k}$ and a pressure sensor in $\mathbf{P}_{d_k}$. Frames $\mathcal{F}_{i_{r,k}}$, $\mathcal{F}_{c_k}$ and $\mathcal{F}_{d_k}$ are the frames associated to these sensors, respectively. Frame $\mathcal{F}_{\mathbf{O}}$ is defined with its x-axis vertical, downwards, and with same yaw angle as $\mathcal{F}_{\mathbf{i_{r,1}}}$. In line with the conclusions of Section V-C, the position of the IMUs along the cable is chosen close to the attachment points, in order to obstruct the *sliding ballast* as little as possible.

The pose of the camera frames $\mathcal{F}_{c_1}$ and $\mathcal{F}_{c_2}$ is estimated using the SfM software Colmap [30] with respect to a reference frame $\mathcal{F}_{w_c}$, which is defined arbitrarily. The position of attachment points $\mathbf{O}$ and $\mathbf{E}$ in frames $\mathcal{F}_{c_1}$ and $\mathcal{F}_{c_2}$ respectively is measured at the beginning of the experiment, in order to determine their relative position in $\mathcal{F}_{w_c}$ according to the SfM reconstruction, along the sequence. Since the transformation between frames $\mathcal{F}_{w_c}$ and $\mathcal{F}_{\mathbf{O}}$ is unknown at any time of the sequence, we use the distance between points $\mathbf{O}$ and $\mathbf{E}$ to characterize the estimation error.

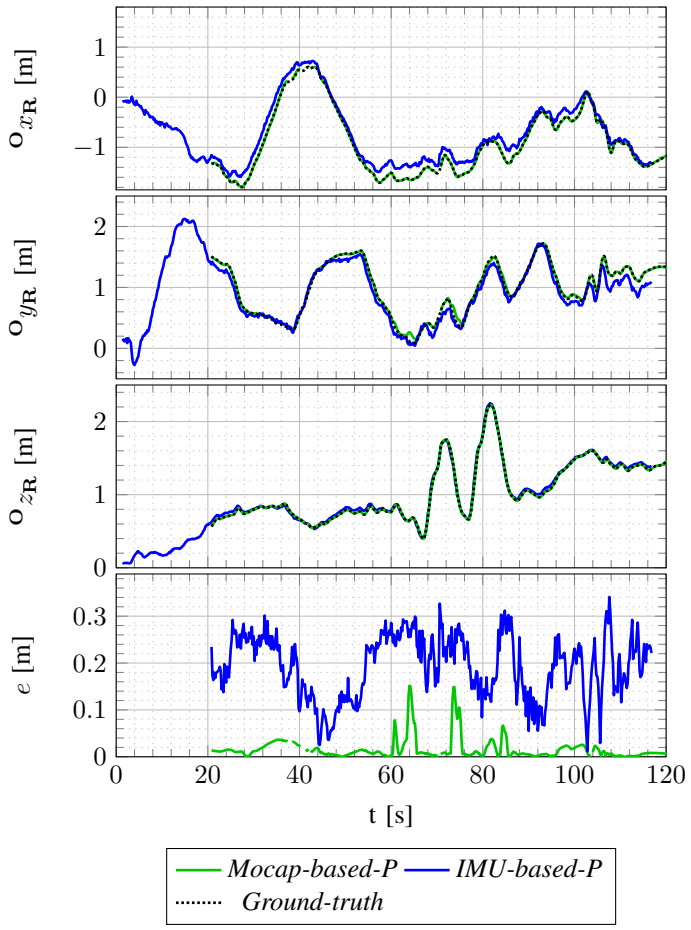

Fig. 13. *IMU-based*, *mocap-based* and *ground truth* ROV position and positioning error for Sequence 5 ($[l_{i_1}, l_{i_2}]$ = [0.40,0.40] m).

A 60 s sequence is recorded. The distance d between attachment points $\mathbf{O}$ and $\mathbf{E}$ computed from the SfM reconstruction and from our localization method and the corresponding error are reported in Figure 16, as well as the distance error e_d defined as the absolute difference between the reference and estimated distance. One can see that the accuracy is about 0.20 m, which is the same order of magnitude as for the system studied in Sections V-B and V-C, featuring a sliding ballast system tethered to a fixed point. Similarly, we can conclude that the current cable-based ROV localization system can also be used in estimating the relative localization of a pair of ROVs tethered by a cable equipped with a sliding ballast.

E. Influence of parameters measurement error

Sections V-B, V-C and V-D demonstrate the interest of the proposed cable-based localization method for operational applications, but also that its accuracy is directly impacted by the accuracy of parameters measurements. An analysis of the influence of embedded sensor-based parameter measurement errors and cable length measurement error is therefore provided in the current section.

1) IMU-based angle measurement errors: For any angle $\gamma \in \{\alpha, \beta, \mu, \eta\}$, we define $\gamma(t)$ the value of the angle at time t and $\hat{\gamma}(t)$ the value measured by the embedded sensors for angle θ. The measurement error on θ at time t is then $e_\theta(t) = \hat{\theta}(t) - \theta(t)$.

Angle measurement error is computed over Sequences 1 to 5 for IMU-based measurements of angles $\{\alpha, \beta, \mu, \eta\}$, using the ground truth angle value θ reported by the motion capture system. The mean μ_θ and standard deviation σ_θ for $\theta \in \{\alpha, \beta, \mu, \eta\}$ are given in Table IV.

TABLE IV
MEAN AND STANDARD DEVIATION OF IMU-BASED ANGLE MEASUREMENT ERRORS

	e_α	e_β	e_μ	e_η
μ_γ (°)	-0.461	-0.077	0.408	0.945
σ_γ (°)	3.673	5.081	3.174	4.982

By combining the errors on angles $\{\alpha, \beta, \mu, \eta\}$, the global mean error of angle measurement μ_{angle} and the global standard deviation of angle measurement σ_{angle} are determined. One gets:

$$\mu_{\text{angle}} = 0.183°$$
$$\sigma_{\text{angle}} = 4.266°$$

In order to study the effect of this noise on the ROV position error, we model the IMU-based angle measurement as:

$$\hat{\gamma}(t) = \gamma(t) + \epsilon \tag{45}$$

where ϵ is a noise. As in [1], two noise models are considered: a Gaussian noise such that $\epsilon = \epsilon_G$ where $\epsilon_G \sim \mathcal{N}(\mu_{\text{angle}}, \sigma^2_{\text{angle}})$ and a uniform noise such that $\epsilon = \epsilon_U$ where $\epsilon_U \sim \mathcal{U}(\mu_{\text{angle}} - 3\sigma_{\text{angle}}, \mu_{\text{angle}} + 3\sigma_{\text{angle}})$. The effect of these two noise models on ROV localization is estimated by adding a random noise ϵ_G or ϵ_U to the ground truth angles measured by the mocap system during Sequences 1 to 5. The mean $\overline{e}$ and standard deviation σ_e obtained for the position error e for each noise model is reported in Table V. These computations use the ground truth value of model parameter $^{\mathbf{O}}z_{\mathbf{E}}$. One can see that these values have the same order of magnitude than the error observed with the IMU measurements and reported in Table III. The error corresponding to the uniform noise is approximately twice higher than the one generated with the Gaussian noise, from about 20 cm to 40 cm for the mean value. The error obtained with the Gaussian noise is however closer to the error observed using IMU measurements and given in Table III, with an order of magnitude of about 20 cm for error mean and of 10 cm for the standard deviation. The Gaussian noise models seems therefore more accurate.

TABLE V
MEAN AND STANDARD DEVIATION WITH SIMULATED ANGLE MEASUREMENT ERRORS

Noise model	ϵ_G	ϵ_U
$\overline{e}$ (m)	0.216	0.385
σ_e (m)	0.105	0.149

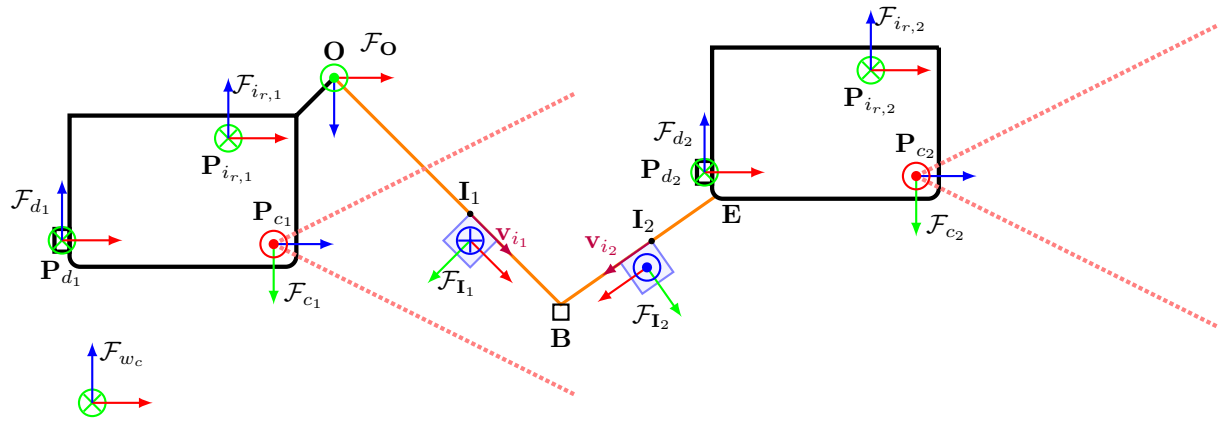

Fig. 14. Two-agent robot chain with a sliding ballast

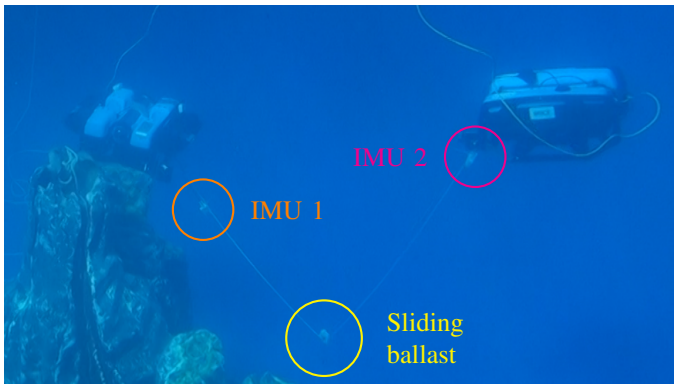

Fig. 15. Robotic system in the pool, featuring two BlueROV2 linked by a cable on which are place a sliding ballast and two IMUs. robots move around a fake reef which is used to compute the SfM baseline.

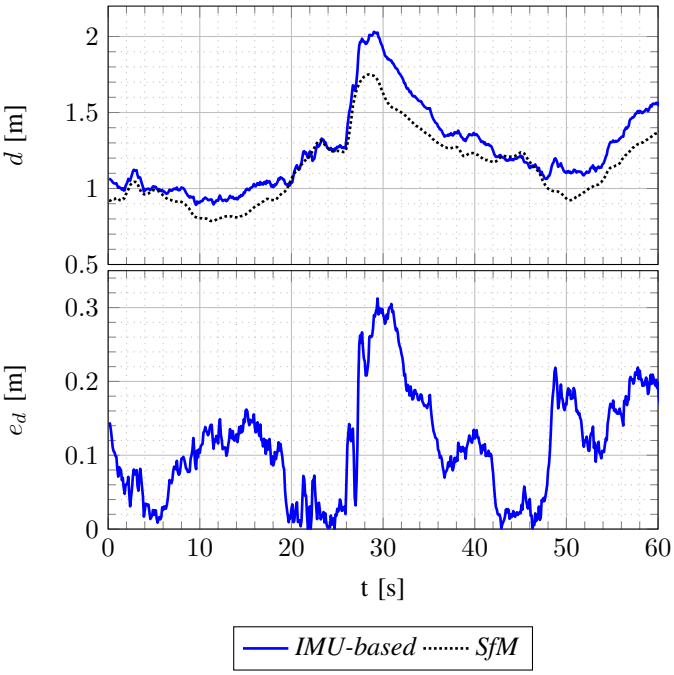

Fig. 16. Relative distance estimation result.

2) Depth measurement error: As in Section V-E1, the error on depth measurement is characterized in order to study the effect of depth measurement noise on the final ROV position estimation. As for angle measurements, we define ${}^{\mathbf{O}}z_{\mathbf{E}}(t)$ the value of ${}^{\mathbf{O}}z_{\mathbf{E}}$ at time t, and ${}^{\mathbf{O}}\hat{z}_{\mathbf{E}}(t)$ the value measured by the embedded sensors. The error on ${}^{\mathbf{O}}z_{\mathbf{E}}$ is denoted e_z and defined such that $e_z(t) = {}^{\mathbf{O}}\hat{z}_{\mathbf{E}}(t) - {}^{\mathbf{O}}z_{\mathbf{E}}(t)$. This error is computed on Sequences 1 to 5, leading to a mean value μ_z and a standard deviation σ_z such that:

$$\mu_z = -0.030 \text{ m}$$
$$\sigma_z = 0.048 \text{ m}$$

As in Section V-E1, the effect of measurement noise on ${}^{\mathbf{O}}z_{\mathbf{E}}$ is evaluated using two noise models parameterized with μ_z and σ_z:

$${}^{\mathbf{O}}\hat{z}_{\mathbf{E}}(t) = {}^{\mathbf{O}}z_{\mathbf{E}}(t) + \epsilon_G \tag{46}$$

where $\epsilon_G \sim \mathcal{N}(\mu_z, \sigma_z^2)$ and

$${}^{\mathbf{O}}\hat{z}_{\mathbf{E}}(t) = {}^{\mathbf{O}}z_{\mathbf{E}}(t) + \epsilon_U \tag{47}$$

where $\epsilon_U \sim \mathcal{U}(\mu_z - 3\sigma_z, \mu_z + 3\sigma_z)$. The addition of a random noise ϵ_G or ϵ_U to the ground truth value of ${}^{\mathbf{O}}z_{\mathbf{E}}$ measured by the mocap during Sequences 1 to 5 leads to a mean error $\bar{e}$ and error standard deviation σ_e given in Table VI. The angles used in these computations are the ground truth values recorded with the motion capture system. It can be observed that these values are significantly lower than those reported in Table V for angle measurement noise. The effect of depth measurement noise is therefore negligible compared to the effect of IMU-based angle measurement noise.

TABLE VI
MEAN AND STANDARD DEVIATION WITH SIMULATED ${}^{\mathbf{O}}z_{\mathbf{E}}$ MEASUREMENT ERRORS

Noise model	ϵ_G	ϵ_U
$\bar{e}$ (m)	0.054	0.082
σ_e (m)	0.034	0.045

3) Umbilical length error: The influence of umbilical length measurement error e_L is studied, such that the measured length is $\hat{L} = L + e_L$. Figure 17 represents the impact of an umbilical length measurement error between -0.5 m and 0.5 m, with an ideal measurement of all other parameters which is given by the mocap system. The average error in Sequences 1 to 5 is indicated, as well as error variance. One can observe that the average errors increase proportionally and with the same order of magnitude as the umbilical measurement error: a measurement error of 1 cm will result in a localization error close to 1 cm, which makes this method robust to small measurement error. For the cable of length $l = 3$ m used in the current experiments, a 1 cm length measurement accuracy can be guaranteed.

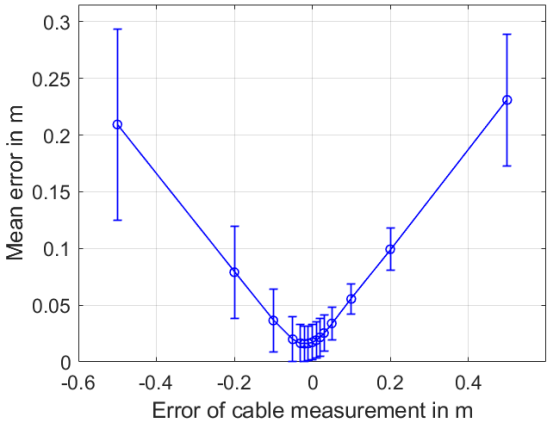

Fig. 17. Effect of cable measurement error e_L on mean ROV localization error $\bar{e}$ for $e_L \in [-0.5, -0.2, -0.1, -0.05, -0.03, -0.02, -0.01, 0, 0.01, 0.02, 0.03, 0.05, 0.1, 0.2, 0.5]$ m.

4) Conclusion on the influence of measurement errors: In the experimental conditions under study, the IMU-based angle measurement errors have been evaluated to cause a ROV localization error of about 20 cm mean and 10 cm standard deviation for the system under study, with a 3 m-long cable. Depth measurement errors have a lower effect on the errors, with a mean value between 5 cm and 10 cm depending on the noise model used, and about 4 cm standard deviation. Finally, the impact of umbilical length error is significantly lower, leading to only 1 cm error with an measurement accuracy of 1 cm, what is easily achievable for the 3 m-long cable used in the experiments. In conclusion, the main source of errors in the proposed ROV localization system lies in the accuracy of the IMU-based angle measurement. This accuracy may nonetheless be improved in several ways. First, in open water, magnetometer data would be available and allow a more accurate yaw angle estimation. In addition, other IMU measurement filters or IMU fixation systems along the cable may be investigated.

F. Influence of the pulley model

For each of the six experimental sequences considered considered in Section V, we compare the results obtained using the cable model described in the current paper, which includes a model that takes the pulley into account, to the cable model used in [1] that does not. These models are denoted *P-model* and *NP-model* respectively. The *NP-model* can be assimilated to a *P-model* with a zero pulley radius. Table VII gives the mean, median and standard deviation of the ROV position error e obtained with the *P* and *NP* models in Sequences 1 to 5, and Table VIII indicates mean, median and standard deviation of the distance error e_d given by the two models on the robot chain sequence.

TABLE VII
STATISTICS ON ERROR e FOR *P* AND *NP* MODELS FOR SEQUENCES 1-5

		Mocap-based		*IMU-based*	
		NP	*P*	*NP*	*P*
Seq. #1	mean (m)	0.011	0.004	0.112	0.125
	median (m)	0.011	0.004	0.110	0.124
	σ (m)	0.001	0.001	0.017	0.017
Seq. #2	mean (m)	0.011	0.017	0.161	0.175
	median (m)	0.007	0.015	0.156	0.172
	σ (m)	0.014	0.015	0.057	0.057
Seq. #3	mean (m)	0.017	0.015	0.173	0.179
	median (m)	0.014	0.012	0.168	0.175
	σ (m)	0.017	0.019	0.090	0.090
Seq. #4	mean (m)	0.016	0.012	0.171	0.178
	median (m)	0.015	0.011	0.150	0.159
	σ (m)	0.008	0.008	0.089	0.089
Seq. #5	mean (m)	0.017	0.015	0.201	0.191
	median (m)	0.013	0.008	0.206	0.196
	σ (m)	0.021	0.022	0.069	0.064

TABLE VIII
COMPARISON BETWEEN THE ERROR e_d FOR THE *P* AND *NP* MODELS FOR THE ROBOT CHAIN SEQUENCE

	IMU-based	
	NP	*P*
mean (m)	0.102	0.114
median (m)	0.093	0.110
σ (m)	0.070	0.074

One can see that the *P-model* is slightly more accurate than the *NP-model* when using mocap-based parameter measurements, in four sequences out of five. However, the *NP-model* slightly outperforms the *P-model* when using embedded sensor-based parameter measurements. As a result, the *P-model* seems to improve the ROV localization estimation only if the model parameters are known very accurately, but the improvement remains marginal.. When the parameters are measured from the embedded sensor, measurements are not accurate enough to observe any improvement when using the *P-model* since the main source of imprecision lies in parameter measurement noise, and not in model approximations. While the *P-model* does not improve the IMU-based localization of the systems considered in Section V, it may however become more valuable for a system featuring a larger pulley, for instance for managing a thicker cable.

VI. DISCUSSION AND PERSPECTIVES

A. Influence of dynamics and waves

The ROV localization method proposed in this paper requires that the cable be kept taut by the ballast, or by the

buoy in the reversed configuration. However, each time the robot moves up, down or back, a part of the tether becomes temporarily loose. A similar behavior can be observed in the presence of waves. To counteract these effects and keep the cable stretched, the ballast must be chosen to dive faster than the descent of the ROV or the waves. Since a heavy ballast would induce a significant drag force on the umbilical, it is recommended to limit the robot velocity such as it moves slower than the ballast. These solutions are discussed in more details in [27].

B. Choice of ballast parameters

To meet Assumption A1, the ballast mass or buoy volume must be chosen to have a faster mechanical response than the cable. A complete study is available in [27, Section 9] and provides a solution according to the umbilical and waves parameters. The drag force induced by the ballast can also be estimated, as described in [27].

C. Interest of the pulley model

The pulley model introduced in this work gives a more accurate description of the cable shape than previous work [1] by taking into account its local deformation at the vicinity of the pulley. However, the use of the pulley model will not improve ROV localization accuracy if measurement error in the model's parameters predominates. In addition, the larger the pulley, the more significant the ROV localization accuracy improvement using the pulley model. The pulley model may also become more worthwhile with more accurate cable angle measurements, which may be obtained, for instance, in open water with magnetometer data available.

D. Geo-referenced localization

If linked to a geo-referenced surface station, the ROV can be geo-referenced using the cable-based localization method presented here, which can be particularly useful for underwater scientific exploration, mapping, or when reaching a place of interest.

E. Limitations of the method

Based on the theory and experiments, some limitations can be observed:

1) As already mention in Section III-A, this method is made for short umbilicals of up to 50 m in length. The main source of ROV localization error lies in the accuracy IMU-based cable angle measurements.
2) The presence of the ballast induces a drag force on the umbilical, and so on the robot.
3) Since the umbilical must be stretched to obtain an accurate localization, strong waves and too fast rotations or displacements of the ROV can disturb the localization. However, some solutions are provided in Section VI-B, and it only takes a few seconds of robot standstill to get a correct estimate again.
4) A collision between the umbilical and an obstacle or the seabed can lead to an erroneous localization by bending the cable so that it no longer conforms to the model. Note that collision with an obstacle of known position and shape can be avoided by the operator since the mathematical model provides the shape of the umbilical. Moreover, a collision can be quickly detected by a discrepancy between the localization and the direction control of the robot. Therefore, this method can be used as an entanglement and collision detector if coupled with another localization system like USBL.
5) The present work only considered short cables of 3 m because of the size constraints of operating in pools. A perspective of this work should be to investigate ROV localization accuracy when using longer cables.

VII. Conclusion

This paper considered the localization of a ROV by observing the shape of its umbilical, which is conformed into a predictable shape by a *sliding ballast* which can move freely along it. This shape is composed of two straight lines connected together by a circular arc that follows the shape of the pulley which holds the ballast. The corresponding cable model is parameterized by the local three-dimensional orientation of the cable at each side of the sliding ballast, which can be measured by two IMUs placed on the cable, and by the relative depth of cable ends.

The cable-based ROV localization strategy was implemented on a real robotic system and evaluated in pools using six sequences, which are representative of real ROV use cases. Five sequences were recorded through a ground truth motion capture system, using a ROV tethered to a fixed point. The sixth sequence was recorded using a SfM-based baseline and a pair of ROVs connected by a cable in the context of a robot chain. The influence of cable-IMU position along the cable was found not to affect cable angles measurement accuracy. The ROV localization accuracy using embedded sensors was reported to be about 20 cm for a 3 m-long cable. The main source of ROV localization error was found to be noise from the IMU-based angle measurement. Finally, the model with the pulley did not improve ROV localization significantly, but it could prove useful with larger pulleys or with greater accuracy of model parameters.

The main assets of the proposed cable-based ROV localization method include its use in open water, its very light, cheep instrumentation and very low computational cost compared to usual acoustic-based techniques. In addition, it provides an estimate of the ROV's position and of the three-dimensional shape of its cable. The proposed localization scheme is also independent from the ROV's environment and operation conditions, including stable currents and visual or acoustic disturbances.

Future works will investigate the deployment of the cable-based ROV localization system in open water, where more accurate IMU-based cable angle measurements are

expected in the absence of magnetic disturbances. These evaluations should be carried out with longer cables to check the influence of cable length on localization accuracy. The current cable-based ROV localization may also be fused with other measurements, in order to provide a more accurate ROV localization estimation. To this end, visual, pressure and inertial measurements may be privileged to preserve the low-cost and low-invasive nature of the ROV localization approach.

Lastly, the proposed localization system may be studied for multiple ROVs tethered together as part of a robot chain-based cable management strategy, where n small additional robots are placed on the cable of a ROV and dedicated to cable shape control (see [22], [24]). This cable-based localization estimate may be combined with other sources of positioning information available for only one or a few robots of the chain, for instance a USBL transceiver placed in the ROV at the chain's end.

VIII. Acknowledgment

We acknowledge support from the Laboratoire de COnception de Systèmes Mécaniques et Robotiques (COSMER), France, the Centre National de la Recherche Scientifique (CNRS), France, the Laboratoire des Sciences et Techniques de l'Information, de la Communication et de la Connaissance (Lab-STICC), France and the Ifremer, La Seyne-sur-mer, France.

References

[1] C. Viel, J. Drupt, C. Dune, and V. Hugel, "Rov localization based on umbilical angle measurement," *Ocean Engineering*, vol. 269, p. 113570, 2023. [Online]. Available: https://www.sciencedirect.com/science/article/pii/S0029801822028530

[2] K. M. Awan, P. A. Shah, K. Iqbal, S. Gillani, W. Ahmad, and Y. Nam, "Underwater wireless sensor networks: A review of recent issues and challenges," *Wireless Communications and Mobile Computing*, vol. 2019, pp. 1–20, Jan. 2019. [Online]. Available: https://doi.org/10.1155/2019/6470359

[3] X. Su, I. Ullah, X. Liu, and D. Choi, "A review of underwater localization techniques, algorithms, and challenges," *Journal of Sensors*, vol. 2020, pp. 1–24, Jan. 2020. [Online]. Available: https://doi.org/10.1155/2020/6403161

[4] D. Park, K. Kwak, J. Kim, and W. K. Chung, "3d underwater localization scheme using em wave attenuation with a depth sensor," in *2016 IEEE International Conference on Robotics and Automation (ICRA)*, 2016, pp. 2631–2636.

[5] D. Park, J. Jung, K. Kwak, W. K. Chung, and J. Kim, "3d underwater localization using em waves attenuation for uuv docking," in *2017 IEEE Underwater Technology (UT)*, 2017, pp. 1–4.

[6] H. Liu, Z. Wang, R. Shan, K. He, and S. Zhao, "Research into the integrated navigation of a deep-sea towed vehicle with usbl/dvl and pressure gauge," *Applied Acoustics*, vol. 159, p. 107052, 2020. [Online]. Available: https://www.sciencedirect.com/science/article/pii/S0003682X18310193

[7] Y. Zhu, T. Zhang, S. Xu, H.-S. Shin, P. Li, B. Jin, L. Zhang, C. Weng, and Y. Li, "A calibration method of usbl installation error based on attitude determination," *IEEE Transactions on Vehicular Technology*, vol. 69, no. 8, pp. 8317–8328, 2020.

[8] M. Audric, "Gaps, a new concept for usbl [global acoustic positioning system for ultra short base line positioning]," in *Oceans '04 MTS/IEEE Techno-Ocean '04 (IEEE Cat. No.04CH37600)*, vol. 2, 2004, pp. 786–788 Vol.2.

[9] F. Mandić, I. Rendulić, N. Mišković, and Đ. Nađ, "Underwater object tracking using sonar and USBL measurements," *Journal of Sensors*, vol. 2016, pp. 1–10, 2016. [Online]. Available: https://doi.org/10.1155/2016/8070286

[10] L. Beaudoin and L. Avanthey, "Underwater field equipment of a network of landmarks optimized for automatic detection by ai," in *IGARSS 2020 - 2020 IEEE International Geoscience and Remote Sensing Symposium*, 2020, pp. 1572–1575.

[11] X. Zhang, H. Guo, J. Mariani, and L. Xiao, "U-star: An underwater navigation system based on passive 3d optical identification tags," in *Proceedings of the 28th Annual International Conference on Mobile Computing And Networking*, ser. MobiCom '22. New York, NY, USA: Association for Computing Machinery, 2022, pp. 648–660. [Online]. Available: https://doi.org/10.1145/3495243.3517019

[12] R. G. Duncan, M. E. Froggatt, S. T. Kreger, R. J. Seeley, D. K. Gifford, A. K. Sang, and M. S. Wolfe, "High-accuracy fiber-optic shape sensing," in *Sensor Systems and Networks: Phenomena, Technology, and Applications for NDE and Health Monitoring 2007*, K. J. Peters, Ed. SPIE, Apr. 2007. [Online]. Available: https://doi.org/10.1117/12.720914

[13] S.-C. Yu, J. Yuh, and J. Kim, "Armless underwater manipulation using a small deployable agent vehicle connected by a smart cable," *Ocean Engineering*, vol. 70, pp. 149–159, 2013. [Online]. Available: https://www.sciencedirect.com/science/article/pii/S002980181300245X

[14] C. Xu, J. Chen, D. Yan, and J. Ji, "Review of underwater cable shape detection," *Journal of Atmospheric and Oceanic Technology*, vol. 33, no. 3, pp. 597–606, Mar. 2016. [Online]. Available: https://doi.org/10.1175/jtech-d-15-0112.1

[15] J. E. Frank, R. Geiger, D. R. Kraige, and A. Murali, "Smart tether system for underwater navigation and cable shape measurement," 2013, uS Patent 8,437,979, URL https://patents.google.com/patent/US8437979B2/en.

[16] B. Buckham and M. Nahon, "Dynamics simulation of low tension tethers," in *Oceans '99. MTS/IEEE. Riding the Crest into the 21st Century. Conference and Exhibition. Conference Proceedings (IEEE Cat. No.99CH37008)*, vol. 2, 1999, pp. 757–766 vol.2.

[17] F. GonzÃ¡lez, A. de la Prada, A. Luaces, and M. GonzÃ¡lez, "Real-time simulation of cable pay-out and reel-in with towed fishing gears," *Ocean Engineering*, vol. 131, pp. 295–307, 2017. [Online]. Available: https://www.sciencedirect.com/science/article/pii/S002980181730001X

[18] S. M. Hong, K. N. Ha, and J.-Y. Kim, "Dynamics modeling and motion simulation of usv/uuv with linked underwater cable," *Journal of Marine Science and Engineering*, vol. 8, no. 5, 2020. [Online]. Available: https://www.mdpi.com/2077-1312/8/5/318

[19] O. A. Eidsvik and I. SchjÃžlberg, "Time domain modeling of rov umbilical using beam equations," *IFAC-PapersOnLine*, vol. 49, no. 23, pp. 452–457, 2016, 10th IFAC Conference on Control Applications in Marine SystemsCAMS 2016. [Online]. Available: https://www.sciencedirect.com/science/article/pii/S2405896316320353

[20] O. Blintsov, "Development of the mathematical modeling method for dynamics of the flexible tether as an element of the underwater complex," *Eastern-European Journal of Enterprise Technologies*, vol. 1, no. 7 (85), pp. 4–14, Feb. 2017. [Online]. Available: https://doi.org/10.15587/1729-4061.2017.90291

[21] O. A. NÃžrve Eidsvik and I. SchjÃžlberg, "Finite element cable-model for remotely operated vehicles (rovs) by application of beam theory," *Ocean Engineering*, vol. 163, pp. 322–336, 2018. [Online]. Available: https://www.sciencedirect.com/science/article/pii/S002980181831014X

[22] M. Laranjeira, C. Dune, and V. Hugel, "Catenary-based visual servoing for tether shape control between underwater vehicles," *Ocean Engineering*, vol. 200, p. 107018, 2020. [Online]. Available: https://www.sciencedirect.com/science/article/pii/S0029801820300949

[23] D. S. D'Antonio, G. A. Cardona, and D. Saldaña, "The catenary robot: Design and control of a cable propelled by two quadrotors," *IEEE Robotics and Automation Letters*, vol. 6, no. 2, pp. 3857–3863, 2021.

[24] J. Drupt, C. Dune, A. I. Comport, S. Seillier, and V. Hugel, "Inertial-measurement-based catenary shape estimation of underwater cables for tethered robots," in *2022 IEEE/RSJ International Conference on Intelligent Robots and Systems (IROS)*, 2022, pp. 6867–6872.

[25] J. Drupt, C. Dune, A. I. Comport, and V. Hugel, "Validity of the catenary model for moving submarine cables with negative buoyancy," in *3rd workshop on RObotic MAnipulation of Deformable Objects: challenges in perception, planning and control for Soft Interaction (ROMADO-SI)*, 2022.

[26] P. McGarey, K. MacTavish, F. Pomerleau, and T. D. Barfoot, "Tslam: Tethered simultaneous localization and mapping for mobile robots," *The International Journal of Robotics Research*, vol. 36, no. 12, pp. 1363–1386, 2017. [Online]. Available: https://doi.org/10.1177/0278364917732639

[27] C. Viel, "Self-management of the umbilical of a rov for underwater exploration," *Ocean Engineering*, vol. 248, p. 110695, 2022.

[Online]. Available: https://www.sciencedirect.com/science/article/pii/S0029801822001494
[28] ——, "Self-management of rov umbilical using sliding buoys and stop," *IEEE Robotics and Automation Letters*, vol. 7, no. 3, pp. 8061–8068, 2022.
[29] S. O. H. Madgwick, S. Wilson, R. Turk, J. Burridge, C. Kapatos, and R. Vaidyanathan, "An extended complementary filter for full-body marg orientation estimation," *IEEE/ASME Transactions on Mechatronics*, vol. 25, no. 4, pp. 2054–2064, 2020.
[30] J. L. Schönberger and J.-M. Frahm, "Structure-from-motion revisited," in *2016 IEEE Conference on Computer Vision and Pattern Recognition (CVPR)*, 2016, pp. 4104–4113.

APPENDIX

A. Calculation of $\hat{L}$

As illustrated on the Figure 3, since $\mathbf{AB}_1$ and $\mathbf{B}_2\mathbf{E}$ are tangent to the circle $\mathcal{C}$, two rectangular triangles $\mathbf{BCB}_1$ and $\mathbf{BCB}_2$ can be defined, with angles $\widehat{\mathbf{BB}_1\mathbf{B}} = \widehat{\mathbf{CB}_2\mathbf{B}} = \frac{\pi}{2}$. Let us define angle θ such that:

$$\theta = \sigma + \psi \tag{48}$$

where $\widehat{\mathbf{B}_1\mathbf{BC}} = \sigma$ and $\widehat{\mathbf{B}_2\mathbf{BC}} = \psi$.

Since $\mathbf{BCB}_1$ and $\mathbf{BCB}_2$ are rectangular, then

$$\widehat{\mathbf{BCB}_1} = \bar{\sigma} \tag{49}$$
$$= \frac{\pi}{2} - \sigma \tag{50}$$

and

$$\widehat{\mathbf{BCB}_2} = \bar{\psi} \tag{51}$$
$$= \frac{\pi}{2} - \psi \tag{52}$$

and so it can be defined

$$\bar{\theta} = \widehat{\mathbf{B}_1\mathbf{CB}_2} \tag{53}$$
$$= \pi - (\sigma + \psi) \tag{54}$$

The length of the arc $\overset{\frown}{\mathbf{B}_1\mathbf{B}_2}$ can be evaluated such that $\overset{\frown}{\mathbf{B}_1\mathbf{B}_2} = l_p = r\bar{\theta}$, and remark $\overset{\frown}{\mathbf{B}_1\mathbf{B}_2} = 0$ when $\bar{\theta} = 0$, *i.e.* the cable is horizontal.

One has $\|\mathbf{B}_1\mathbf{C}\| = \|\mathbf{B}_2\mathbf{C}\| = r$ because are radius of $\mathcal{C}$. Thus, one gets

$$l_{p_1} = \|\mathbf{B}_1\mathbf{B}\| = r\tan(\bar{\sigma}) \tag{55}$$
$$l_{p_2} = \|\mathbf{B}_2\mathbf{B}\| = r\tan(\bar{\psi}) \tag{56}$$

Finally, since the rectangular triangles $\mathbf{BCB}_1$ and $\mathbf{BCB}_2$ have a common side $\mathbf{BC}$ and $\|\mathbf{B}_1\mathbf{C}\| = \|\mathbf{B}_2\mathbf{C}\| = r$, thus the third sides $\mathbf{BB}_1$ and $\mathbf{BB}_2$ of each triangle have the same length (Pythagore theorem), *i.e.* $\|\mathbf{BB}_1\| = \|\mathbf{BB}_2\|$. Thus, $\frac{\|\mathbf{BB}_1\|}{\|\mathbf{B}_1\mathbf{C}\|} = \frac{\|\mathbf{BB}_2\|}{\|\mathbf{B}_2\mathbf{C}\|} \Leftrightarrow \cos(\sigma) = \cos(\psi)$ and so $\sigma = \psi$. Since $\theta = \sigma + \psi$, one gets $\sigma = \psi = \frac{\theta}{2}$, then $\bar{\theta} = \pi - \theta$ and

$$l_{p1} = \tan\left(\frac{\pi - \theta}{2}\right) r \tag{57}$$
$$l_{p2} = \tan\left(\frac{\pi - \theta}{2}\right) r \tag{58}$$

Finally, $\hat{L}$ can be expressed as

$$\hat{L} = l_1 + l_2 \tag{59}$$
$$= l_{c_1} + l_{c_2} + l_{p1} + l_{p2} \tag{60}$$
$$= L_c - l_p + 2\tan\left(\frac{\pi - \theta}{2}\right) r \tag{61}$$
$$= L_c - r(\pi - \theta) + 2\tan\left(\frac{\pi - \theta}{2}\right) r \tag{62}$$

Note that when the cable is folded, one has $\theta = 0$ and so $\hat{L}$ tends to infinity: to solve this particular case, a saturation $\hat{L} > L_{\text{max}}$ for a defined L_{max} is defined. On can take $L_{\text{max}} = L$.

B. Calculation of l_{1_x}, l_{2_x} and l_{1_y}, l_{2_y}

Let define ${}^{\mathbf{O}}z_{\mathbf{B}}$ the z-coordinate of $\mathbf{B}$ in $\mathcal{F}_{\mathbf{O}}$. Since ${}^{\mathbf{O}}z_{\mathbf{B}}$ can be evaluated in the plans $(\mathbf{O}, \mathbf{x_O}, \mathbf{z_O})$ and $(\mathbf{O}, \mathbf{y_O}, \mathbf{z_O})$, one has

$${}^{\mathbf{O}}z_{\mathbf{B}} = l_0 + s_b l_{1_x}\cos(\alpha) = l_0 + s_b l_{1_y}\cos(\mu) \tag{63}$$
$${}^{\mathbf{O}}z_{\mathbf{B}} = {}^{\mathbf{O}}z_{\mathbf{E}} - s_b l_{2_x}\cos(\beta) = {}^{\mathbf{O}}z_{\mathbf{E}} - s_b l_{2_x}\cos(\eta) \tag{64}$$

where ${}^{\mathbf{O}}z_{\mathbf{E}}$ is the z-coordinate of $\mathbf{E}$ in $\mathcal{F}_{\mathbf{O}}$. Using (63)-(64), one gets

$$l_{1_x} = l_{1_y}\frac{\cos(\mu)}{\cos(\alpha)} \tag{65}$$
$$l_{2_x} = l_{2_y}\frac{\cos(\eta)}{\cos(\beta)}. \tag{66}$$

In addition,

$$l_1^2 = l_{1_x}^2 + \sin(\mu)^2 l_{1_y}^2 \tag{67}$$
$$l_2^2 = l_{2_x}^2 + \sin(\eta)^2 l_{2_y}^2 \tag{68}$$

Using (65) and (67), one gets

$$\begin{aligned} l_1^2 &= l_{1_x}^2 + \sin(\mu)^2 l_{1_y}^2 \\ l_1^2 &= l_{1_x}^2 + \sin(\mu)^2 \left(\frac{\cos(\alpha)}{\cos(\mu)}\right)^2 l_{1_x}^2 \\ l_1^2 &= \left(1 + \tan(\mu)^2\cos(\alpha)^2\right) l_{1_x}^2 \\ l_{1_x}^2 &= \frac{l_1^2}{\left(1 + \tan(\mu)^2\cos(\alpha)^2\right)}. \end{aligned} \tag{69}$$

In the same way, one can obtain using again (65) and (67)

$$\begin{aligned} l_1^2 &= l_{1_x}^2 + \sin(\mu)^2 l_{1_y}^2 \\ l_1^2 &= l_{1_y}^2 \left(\frac{\cos(\mu)}{\cos(\alpha)}\right)^2 + \sin(\mu)^2 l_{1_y}^2 \\ l_{1_y}^2 &= \frac{l_1^2}{\left(\sin(\mu)^2 + \left(\frac{\cos(\mu)}{\cos(\alpha)}\right)^2\right)}. \end{aligned} \tag{70}$$

Same calculation can be made for $l_{2_x}^2$, l_{2z}^2 using respectively (66)-(68), leading to

$$l_{2_x}^2 = \frac{l_2^2}{\left(1+\tan\left(\eta\right)^2\cos\left(\beta\right)^2\right)} \tag{71}$$

$$l_{2_y}^2 = \frac{l_2^2}{\left(\sin\left(\eta\right)^2+\left(\frac{\cos(\eta)}{\cos(\beta)}\right)^2\right)}. \tag{72}$$

C. Calculation of l_1 and l_2

The z-coordinate of $\mathbf{E}$ in $\mathcal{F}_\mathbf{O}$ is such that:

$$\begin{cases} {}^\mathbf{O}z_\mathbf{E} = & l_0 + s_b l_{1_x}\cos\left(\alpha\right) - s_b l_{2_x}\cos\left(\beta\right) \\ {}^\mathbf{O}z_\mathbf{E} = & l_0 + s_b l_{1_y}\cos\left(\mu\right) - s_b l_{2_y}\cos\left(\eta\right) \end{cases} \tag{73}$$

an therefore

$$s_b\left({}^\mathbf{O}z_\mathbf{E} - l_0\right) = l_{1_x}\cos\left(\alpha\right) - l_{2_x}\cos\left(\beta\right) \tag{74}$$

since $s_b \in \{-1, 1\}$.

Introducing (69) and (71), one gets

$$s_b\left({}^\mathbf{O}z_\mathbf{E} - l_0\right) = \frac{l_1\cos\left(\alpha\right)}{a_1} - \frac{l_2\cos\left(\beta\right)}{a_2}. \tag{75}$$

where

$$a_1 = \sqrt{1+\tan\left(\mu\right)^2\cos\left(\alpha\right)^2}$$
$$a_2 = \sqrt{1+\tan\left(\eta\right)^2\cos\left(\beta\right)^2}$$

Since $\hat{L} = l_1 + l_2$, (75) becomes

$$s_b\left({}^\mathbf{O}z_\mathbf{E} - l_0\right) = \frac{\hat{L}\cos\left(\alpha\right)}{a_1} - l_2\left(\frac{\cos\left(\alpha\right)}{a_1} + \frac{\cos\left(\beta\right)}{a_2}\right)$$
$$l_2 = \frac{\frac{\hat{L}\cos(\alpha)}{a_1} - s_b\left({}^\mathbf{O}z_\mathbf{E} - l_0\right)}{\frac{\cos(\alpha)}{a_1} + \frac{\cos(\beta)}{a_2}} \tag{76}$$

and so

$$l_1 = \hat{L} - \frac{\frac{\hat{L}\cos(\alpha)}{a_1} - s_b\left({}^\mathbf{O}z_\mathbf{E} - l_0\right)}{\frac{\cos(\alpha)}{a_1} + \frac{\cos(\beta)}{a_2}}. \tag{77}$$

D. Calculation of θ

Let $\begin{bmatrix}{}^\mathbf{O}x_1 & {}^\mathbf{O}y_1 & {}^\mathbf{O}z_1\end{bmatrix}^T$ and $\begin{bmatrix}{}^\mathbf{O}x_2 & {}^\mathbf{O}y_2 & {}^\mathbf{O}z_2\end{bmatrix}^T$ denote the coordinates of vectors $\mathbf{AB}$ and $\mathbf{BE}$ respectively, in frame $\mathcal{F}_\mathbf{O}$. One gets

$$\begin{bmatrix}{}^\mathbf{O}x_1 \\ {}^\mathbf{O}y_1 \\ {}^\mathbf{O}z_1\end{bmatrix} = \begin{bmatrix}\frac{l_1\sin(\alpha)}{a_1} \\ \frac{l_1\sin(\mu)}{a_3} \\ s_b\frac{l_1\cos(\alpha)}{a_1}\end{bmatrix} \tag{78}$$

and

$$\begin{bmatrix}{}^\mathbf{O}x_2 \\ {}^\mathbf{O}y_2 \\ {}^\mathbf{O}z_2\end{bmatrix} = \begin{bmatrix}-\frac{l_2\sin(\beta)}{a_2} \\ -\frac{l_2\sin(\eta)}{a_4} \\ s_b\frac{l_1\cos(\beta)}{a_2}\end{bmatrix} \tag{79}$$

where a_1, a_2, a_3 and a_4 are defined in (20), (21), (23) and (24) respectively. $\theta = \widehat{\mathbf{ABE}}$ can be expressed as:

$$\theta = \arccos\left(\frac{\mathbf{AB}\cdot\mathbf{BE}}{\|\mathbf{AB}\|\|\mathbf{BE}\|}\right) \tag{80}$$

where $(\cdot)$ denotes the Euclidian scalar product. Finally, one gets

$$\theta = \arccos\left(\frac{\cos(\alpha+\beta)}{a_1 a_2} - \frac{\sin(\mu)\sin(\eta)}{a_3 a_4}\right) \tag{81}$$

E. Calculation of $d_\mathbf{E}$

Let $P_\mathbf{D}$ denote the water pressure measured at $\mathbf{D}$.

$$P_\mathbf{D} = P_{\text{water}} + P_{atm} + P_b \tag{82}$$

where P_{atm} is the atmospheric pressure, P_b is a sensor bias, and P_{water} is the pressure exerted by the water column, with:

$$P_{\text{water}} = \rho_{\text{water}} * g * d_\mathbf{D} \tag{83}$$

ρ_{water} is the volumetric mass of water, g is the value of gravity on Earth and $d_\mathbf{D}$ is the depth of measurement point $\mathbf{D}$ with respect to the surface. Let us define $P_0 = P_{atm} + P_b$, which is the pressure returned by the pressure sensor at zero depth. One can get:

$$P_{\text{water}} = \rho_{\text{water}} * g * d_\mathbf{D} - P_0 \tag{84}$$

hence:

$$d_\mathbf{D} = \frac{P_\mathbf{D} - P_0}{\rho_{\text{water}} * g} = \frac{P_\mathbf{D}}{\rho_{\text{water}} * g} + c_2 \tag{85}$$

where $c_2 = \frac{-P_0}{\rho_{\text{water}} * g}$.

Depth at $\mathbf{E}$ can be deduced from $d_\mathbf{D}$ and the rotation matrix ${}^w\mathbf{R}_{\mathbf{I}_r}$. Let us define frame $\mathcal{F}_\mathbf{S}$ with origin the surface point $\mathbf{S}$ located vertically from $\mathbf{D}$ and with same orientation as $\mathcal{F}_w$ (Figure 5).

Depth at $\mathbf{E}$ is then:

$$d_\mathbf{E} = -{}^\mathbf{S}z_\mathbf{E} \tag{86}$$

where ${}^\mathbf{S}z_\mathbf{E}$ is the z-coordinate of $\mathbf{E}$ in $\mathcal{F}_\mathbf{S}$. In homogeneous coordinates, one gets:

$${}^\mathbf{S}\overline{\mathbf{D}} = {}^\mathbf{S}\mathbf{T}_\mathbf{D}\,{}^\mathbf{D}\overline{\mathbf{D}} \tag{87}$$

where ${}^\mathbf{S}\mathbf{T}_\mathbf{D}$ is the rigid transformation between $\mathcal{F}_\mathbf{D}$ et $\mathcal{F}_\mathbf{S}$. According to the definition of frames $\mathcal{F}_\mathbf{D}$, $\mathcal{F}_\mathbf{S}$, $\mathcal{F}_{\mathbf{I}_r}$ and $\mathcal{F}_w$ one gets:

$${}^\mathbf{S}\mathbf{T}_\mathbf{D} = \left[\begin{array}{c|c} {}^\mathbf{S}\mathbf{R}_\mathbf{D} & \begin{matrix}0\\0\\d_\mathbf{D}\end{matrix} \\ \hline \begin{matrix}0 & 0 & 0\end{matrix} & 1\end{array}\right] = \left[\begin{array}{c|c} {}^w\mathbf{R}_{\mathbf{I}_r} & \begin{matrix}0\\0\\d_\mathbf{D}\end{matrix} \\ \hline \begin{matrix}0 & 0 & 0\end{matrix} & 1\end{array}\right] \tag{88}$$

and finally:

$$d_\mathbf{E} = -\begin{bmatrix}0 & 0 & 1 & 0\end{bmatrix}\,{}^\mathbf{S}\mathbf{T}_\mathbf{D}\,{}^\mathbf{D}\overline{\mathbf{E}} \tag{89}$$